Formation and transformation of a short range ordered iron carbonate precursor

Knud Dideriksen[ae], Cathrine Frandsen[b], Nicolas Bovet[a], Adam F.Wallace[c], Ozlem Sel[d], Tyler Arbour[e], Alexandra Navrotsky[f], James J.De Yoreo[g], Jillian F.Banfield[a]
Show more

https://doi.org/10.1016/j.gca.2015.05.005

Abstract

Fe(II)-carbonates, such as siderite, form in environments where O_2 is scarce, e.g., during marine sediment diagenesis, corrosion and possibly CO_2sequestration, but little is known about their formation pathways. We show that early precipitates from carbonate solutions containing 0.1 M Fe(II) with varying pH produced broad peaks in X-ray diffraction and contained dominantly Fe and CO_3 when probed with X-ray photoelectron spectroscopy. Reduced pair distribution function (PDF) analysis shows only peaks corresponding to interatomic distances below 15 Å, reflecting a material with no long range structural order. Moreover, PDF peak positions differ from those for known iron carbonates and hydroxides. Mössbauer spectra also deviate from those expected for known iron carbonates and suggest a less crystalline structure. These data show that a previously unidentified iron carbonate precursor phase formed. Its coherent scattering domains determined from PDF analysis are slightly larger than for amorphous calcium carbonate, suggesting that the precursor could be nanocrystalline. Replica exchange molecular dynamics simulations of Fe-carbonate polynuclear complexes yield PDF peak positions that agree well with those from experiments, offering the possibility that the material is a condensate of such complexes, assembled in a relatively unorganised fashion. If this is the case, the material could be nearly amorphous, rather than being composed of well defined nanocrystals. PDF measurements of samples ageing in solution coupled with refinement with the software PDFgui show that the material transforms to siderite or siderite/chukanovite mixtures within hours and that the transformation rate depends on pH. The identified Fe-carbonate precursor may potentially form during anaerobic corrosion or bacterial Fe reduction.

1. Introduction

Carbonates are among the most common sediments, with Ca- and Mg-carbonates storing the majority of the total carbon in the crust. Through most of Earth's history, these sediments have formed from divalent metals, released from silicate weathering, and from atmospheric CO_2. In the long-term carbon cycle, this process has played a critical role in regulating the atmospheric CO_2 content (e.g., Berner et al., 1983, Berner and Kothavala, 2001). However, natural weathering is relatively slow and the resulting carbonate precipitation cannot counter current anthropogenic emissions.
One method to actively decrease atmospheric emissions is to capture and store CO_2 from point sources such as power plants (for an overview, see Elements, 2008, Vol. 4 (5)). The storage options considered include in-situ mineral carbonation, where CO_2 is injected into highly reactive rock, for

example basalt rich in Ca, Mg and Fe(II), with the specific aim of causing silicate dissolution and carbonate precipitation (e.g., Oelkers et al., 2008, Gislason et al., 2010, Aradóttir et al., 2012, Gislason and Oelkers, 2014). As another storage option, CO_2 could be injected into deep sedimentary formations, such as spent oil and gas reservoirs or formations bearing saline waters. On shorter time scales, the CO_2 would be kept in place by overlying impermeable sediments or by trapping as isolated bubbles left in pore spaces after plume migration (capillary trapping). With time, silicates in the sediment would react with the CO_2 and dissolve. If these minerals are rich in Ca, Mg or Fe(II), carbonates are likely to form. Iron is among the most abundant elements in the crust (e.g., Wedepohl, 1995) and it could contribute significantly to the mineral carbonation capacity. However, Fe(II) oxidises readily to Fe(III) if oxygen is present, impeding the formation of carbonates, and reducing conditions, such as those found in the deep subsurface, are required for Fe(II)-carbonates to form.

There are two known Fe(II)-carbonate minerals, siderite and chukanovite. Siderite ($FeCO_3$) is isostructural with calcite ($CaCO_3$), but has a smaller unit cell, reflecting the smaller effective ionic radius of Fe(II) (0.78 Å for high spin Fe(II), 1.00 Å for Ca(II); Shannon, 1976). Siderite forms readily in anoxic environments with Fe(II) and CO_3^{2-} present, for example during corrosion of metallic Fe (e.g., Neff et al., 2005) or during bacterial reduction of Fe(III)-oxides (Mortimer et al., 1997, Fredrickson et al., 1998, Dong et al., 2000, Liu et al., 2001, Roh et al., 2003, Johnson et al., 2005). Consequently, the mineral occurs throughout the geological record. As a pertinent example, siderite forms during diagenesis of sediments (e.g., Pye, 1984, Ellwood et al., 1988), incorporating trace elements that may reflect the depositional environment (Mozley, 1989), and it is common in banded iron formations, where its presence suggests that Archaean CO_2 partial pressure was relatively high (Ohmoto et al., 2004). Chukanovite ($Fe_2CO_3(OH)_2$) was recently identified as a corrosion product on an iron meteorite (Pekov et al., 2007), but little is known about its occurrence in nature. Laboratory studies indicate that it is metastable with respect to siderite (Azoulay et al., 2012) and that it can form during microbial Fe reduction (Kukkadapu et al., 2005).

Although the Fe-carbonate minerals, especially siderite, are relatively well-described, little is known about precursor phases and possible formation pathways. For Ca-carbonates, an amorphous Ca-carbonate (ACC) precursor exists as a biomineral (e.g., Gilbert and Wilt, 2011 and references therein). In addition, two studies suggest that Ca-carbonate clusters may exist in solution and that these can coalesce to form ACC (Gebauer et al., 2008, Pouget et al., 2009). In recent experiments, Sel et al. (2012) produced hydrated iron carbonate ($FeCO_3 \cdot 1.75H_2O$) that showed no long-range order with X-ray diffraction. The aim of the current study is to probe the structure of this material and to quantify structural and morphological evolution with time and in solutions of varying pH. We tested the hypothesis that the material is a precursor to siderite and/or chukanovite by using X-ray photoelectron spectroscopy, pair distribution function analysis and Mössbauer spectroscopy.

2. Materials and methods

To minimise the oxidation of Fe(II), all synthesis and sample preparation were carried out in anaerobic chambers. The materials which were characterised with laboratory-based techniques were

synthesized in vinyl-walled chambers from Coy Lab, whereas materials characterised by synchrotron radiation were synthesized in a hard-walled chamber from Plas-Labs. The atmosphere in the chambers consisted of about 3% H_2 and 97% N_2 and they were equipped with palladium catalysts on fan boxes for reaction of trace O_2 with H_2 to form water.

All solutions used were de-oxygenated before use. Ultrapure water (resistivity > 18 MΩ cm) was bubbled with N_2 for two hours and then transferred to the anaerobic chamber, whereas organic solvents (ethanol and acetone) were transferred directly. Inside the chamber, the solutions were equilibrated with the atmosphere over two to three days by repeatedly (at least 10 times): (1) uncapping the bottle allowing exchange of gas in the bottle with that of the chamber and (2) capping the bottle and shaking it to equilibrate gas with solution.

Stock solutions were prepared from $NaHCO_3$ (Sigma–Aldrich) and Na_2CO_3(Sigma–Aldrich) salts and NaOH pellets (Sigma–Aldrich) to obtain 0.5 M carbonate solutions and 1 M NaOH solutions. 0.5 M Fe(II) stock solutions were prepared by dissolving $Fe(II)Cl_2{\cdot}4H_2O$ (Sigma–Aldrich) in water inside the anaerobic chamber. To minimise Fe(III) impurities in the solution, a small amount of 1 M NaOH was added to the solution which resulted in a dark green precipitate. The centrifuge tube with the slurry was capped and sealed with parafilm. It was then centrifuged outside the chamber at 6000*g*, transferred back to the chamber and filtered with 0.45 μm filters to produce a clear solution. To minimise Fe(II) oxidation rates, the solution pH was adjusted to 3 with a small amount of 6 M HCl, which resulted in a pale blue solution.

Before use, the stock solutions were tested for the presence of Fe(III) and dissolved O_2. This was done by mixing portions of the Fe(II) stock solution with portions of the carbonate stock solutions to precipitate a small amount of material. Fe(III)-bearing oxides, oxyhydroxides and hydroxides (henceforth simply termed Fe-oxide) are very strongly coloured (Cornell and Schwertmann, 2003) and tint materials even when present in small amounts. Experiments were only conducted if the precipitate was white. Using freshly precipitated Fe(II)-carbonates separated from solution with centrifugation, organic solvents were also tested for the presence of dissolved oxygen prior to the experiments by resuspending the white precipitate in the solvents. Only solvents in which the solid's colour remained unchanged after exposure were used in the experiment.

For Fe(II)-carbonate precipitation, 0.2 M $Fe(II)Cl_2$ and 0.2 M carbonate solutions of equal volumes were prepared from the stock solutions. For most experiments, the solutions were either 0.2 M $NaHCO_3$ or Na_2CO_3, but a few experiments were carried out with mixtures having either (a) 0.1 M $NaHCO_3$and 0.1 M Na_2CO_3 or (b) 0.2 M Na_2CO_3 and 0.2 M NaOH. In addition, $Fe(OH)_2$ was precipitated using 0.2 M NaOH. To initiate precipitation, the $Fe(II)Cl_2$ was poured into base solutions and the mixture was shaken. After precipitation, samples were taken either freshly (within a minute) or after ageing by transferring 12 ml of slurry to 2 ml centrifuge tubes. The tubes were centrifuged for 5 s at 2000*g* to quickly separate solid and solution. In selected experiments, the pH was monitored during the precipitation and samples were taken after one minute for determination of aqueous Fe concentration with atomic absorption spectroscopy (AAnalyst 800; Perkin Elmer Precisely) after centrifugation of the slurry at 14,000*g*.

The solids were characterised either dried, frozen or in solution. For dry samples, the supernatant was discarded and the solid was washed once in ethanol and twice in acetone by resuspending the precipitate in the solvents, followed by centrifugation and removal of supernatant. The precipitate was subsequently resuspended in acetone and transferred to spin columns (Qiagen), which were centrifuged for 15 min at 2000*g* to remove the solvent. This resulted in a pellet of material that could be flattened and dried within 2 min in the chamber. One sample for characterisation with high-energy X-ray diffraction was prepared using vacuum filtration, identical to the procedure used by Sel et al. (2012).

Several methods were used to characterise the dried samples, each with their own sample-preparation protocol intended to minimise oxidation during time of transport (~5 min unless otherwise noted) and analysis. Solids for in-house X-ray diffraction (XRD) were mounted on low-background silica plates, the sample holder was capped with a polymer hemisphere (Bruker), and the analysis was performed immediately. Materials for scanning electron microscopy and energy dispersive X-ray spectroscopy (SEM/EDX) were mounted on Al sample holders and put into centrifuge tubes that were capped inside the anaerobic chamber and taken for coating with gold. During transfer to the sputter coater, samples were exposed to the atmosphere for about 30 s. Material for transmission electron microscopy (TEM) was resuspended in ethanol and 20 µl of the suspension was transferred to a Cu-grid. The grid was transported in a capped container and was transferred to the instrument in about 30 s. Samples for X-ray photoelectron spectroscopy (XPS) were placed into sample holders that were mounted in a transfer chamber inside the anaerobic chamber. The transfer chamber was then taken to the XPS and attached on a flange on the N_2-vented entry chamber. Despite these precautions to minimise the contact with air, some material appeared slightly darkened when observed with the black and white camera in the sample chamber, indicating that some oxidation had occurred during transport to the XPS. Dry solids for characterisation with synchrotron X-rays were transferred to 0.9 mm borosilicate glass (Mark Rörchen) or Kapton (Cole-Parmer) capillary tubes. Glass capillary tubes were sealed with paraffin and samples inside remained white for more than a week. Kapton capillary tubes were sealed with ~7 mm epoxy in one end and with paraffin in the other.

Frozen samples were prepared for Mössbauer spectroscopy by first resuspending the solid in a small amount of supernatant and transferring the slurry to the sample holder within the anaerobic chamber. One sample precipitated from $NaHCO_3$ and $FeCl_2$ was centrifuged, then the supernatant was decanted, and the solid was resuspended in ultrapure water to remove aqueous Fe(II). Upon transfer out of the chamber, the sample holder was immediately dropped into liquid nitrogen to quench reaction and protect the material from oxidation during the transport to the spectrometer.

Samples in solution were prepared for characterisation with synchrotron radiation by first resuspending the centrifuged materials in a small amount of supernatant. Portions of these thick slurries were then transferred to glass capillary tubes so that half of their volume was filled. These were sealed with paraffin, put into 15 ml centrifuge tubes and taken outside the anaerobic chamber for centrifugation with swing-out cups at 2000*g* for 2 min. This resulted in settling of the particles in the bottom 1–2 cm of the capillary tubes, concentrating the solid material.

In-house XRD was carried out on a PANalytical X'Pert PRO diffractometer with a Co cathode operated at 40 kV and 40 mA. The pattern was measured from 10° to 70° or 80° (2θ) without sample spinning. SEM/EDX was performed on an Evo MA 10 using an accelerating voltage of 10 or 30 kV. Probe current was 0.1 nA for regular SEM and 1 nA for SEM/EDX. TEM was carried out on a Phillips CM20 with an accelerating voltage of 200 kV. XPS was performed in a Kratos Axis Ultra^{DLD} fitted with a monochromatic $Al_{K\alpha}$ X-ray source (power = 150 eV). Binding energy calibration was done with the C 1s peak of adventitious carbon at 285 eV. The pass energy used for high-resolution scans was 20 eV. ^{57}Fe Mössbauer spectroscopy was carried out by using constant acceleration spectrometers with ^{57}Co in Rh as sources. The spectrometers were calibrated using a 12.5 μm foil of α-Fe. Spectra were obtained at temperatures of 13–40 K using a closed-cycle helium refrigerator from APD Cryogenics.

Synchrotron X-ray scattering for reduced pair distribution function (PDF) analysis was carried out at Beamline 11-ID-B at the Advanced Photon Source, Argonne National Laboratory. The X-ray wavelength, λ, was 0.2128 Å and scattered X-rays were detected by a ~40 cm by ~40 cm amorphous Si 2D detector (Perkin Elmer) placed ~15 cm from the sample. The setup geometry was calibrated with a CeO_2 standard using Fit-2D (Hammersley et al., 1994, Hammersley, 1997). This software was also used for converting 2D data to polarisation-corrected 1D data, allowing PDFs to be obtained with PDFGETX2 (Chupas et al., 2003, Qiu and Thompson, 2004; manual available at: http://www.pa.msu.edu/cmp/billinge-group/programs/PDFgetX2/download/manual.pdf). Data treatment in PDFGETX2 included standard corrections, such as subtraction of the background (empty capillary tubes for dried samples and water-filled capillary tubes for slurries), subtraction of incoherent scattering, and normalisation by the sample's average atomic scattering cross section, as well as corrections for non-linear detector efficiency. In the treatment, single-phase samples were assumed to have the composition given by their structure. For the initial material and for mixtures, a composition of $FeCO_3 \cdot H_2O$ was assumed. Moderate variation of the water content (±50%) did not affect the resulting PDF significantly. PDFs were acquired from Fourier transform of the reduced scattering structure function, Q[S(Q)−1]. For the initial dried samples, the Q[S(Q)−1] became notably noisier at Q values above ~18.5 $Å^{-1}$. Consequently, PDFs were acquired from Fourier transform of the Q[S(Q)−1] using a maximum Q of 18 $Å^{-1}$ for all dried samples to allow comparison of their patterns. For the samples measured in solution, the solid material was much less densely packed, and the subtraction of a large water background resulted in increased level of noise in the Q[S(Q)−1]. For these samples, the PDFs were generated using a maximum Q of 16 $Å^{-1}$. Real-space fitting of PDFs, analogous to Rietveld refinement, were performed using PDFgui (Farrow et al., 2007) and structural data of siderite (Graf, 1961), chukanovite (Pekov et al., 2007), and amakinite, $Fe(OH)_2$ (Wyckoff, 1963). An instrumental dampening of 0.049 was refined from PDFs of crushed natural siderite and magnetite and synthetic goethite. Parameters were fitted in the order: (1) Scaling, size of coherently scattering domains (assumed spherical) and correlated atomic movement (δ_2), (2) unit cell dimensions, (3) atomic isotropic displacement parameters and (4) Fe occupancy. Atomic positions were not fitted because this typically results in unrealistic changes to the structure of the carbonate group.

3. Results

Mixing of the $FeCl_2$ and carbonate solutions produced a white precipitate within 10 s. In experiments with $NaHCO_3$, the pH of the mixture stabilised at 6.6 after a minute, yielding an Fe concentration of 75 mM. These values agree with those predicted by PHREEQC calculations with the MINTEQ database (Allison et al., 1990, Parkhurst and Appelo, 1999), for $FeCO_3$precipitation in a closed system until supersaturation with respect to siderite by a factor of $10^{2.8}$ is reached.

3.1. Characterisation of initial and aged solids

XRD patterns from the initial solids precipitated with $NaHCO_3$, Na_2CO_3 and an equimolar Na_2CO_3/NaOH mixture (Fig. 1A–C) display 1 or 2 very broad humps (i.e., no sharp Bragg reflections), indicating the absence of long-range ordering. For the precipitates from $NaHCO_3$ solutions, SEM images revealed spherical particles of ~100 nm (Fig. 2A) similar in shape to ACC particles (e.g., Rodriguez-Blanco et al., 2008). The material precipitated from Na_2CO_3solutions had a gel-like consistency after centrifugation and appeared as larger cakes with a rough surface looking somewhat like crumpled paper in SEM (Fig. 2B). The latter precipitate (Fig. 2B) resembled those observed by Konhauser et al. (2007), who probed Fe(II) photo-oxidation to explore the Fe-phases that might have formed in Archaean oceans.

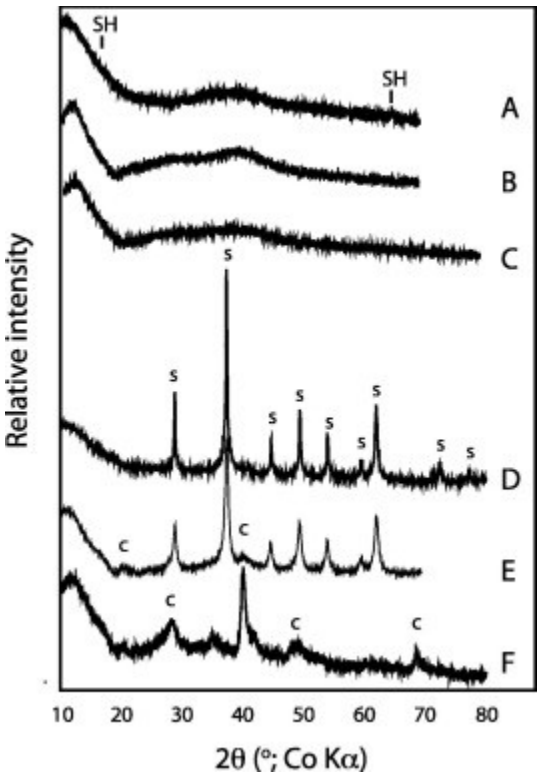

1. Download full-size image

Fig. 1. In-house XRD of initial precipitates from solutions with (A) 0.1 M $NaHCO_3$, (B) 0.1 M Na_2CO_3, (C) 0.1 M Na_2CO_3 and 0.1 M NaOH, and aged precipitates from solutions with (D) 0.1 M $NaHCO_3$ (aged 5 days), (E) 0.1 M Na_2CO_3 (aged 1 month), (F) 0.1 M Na_2CO_3 and 0.1 M NaOH (aged 2 days). Peaks from the sample holder are denoted SH, from siderite, s, and from chukanovite, c.

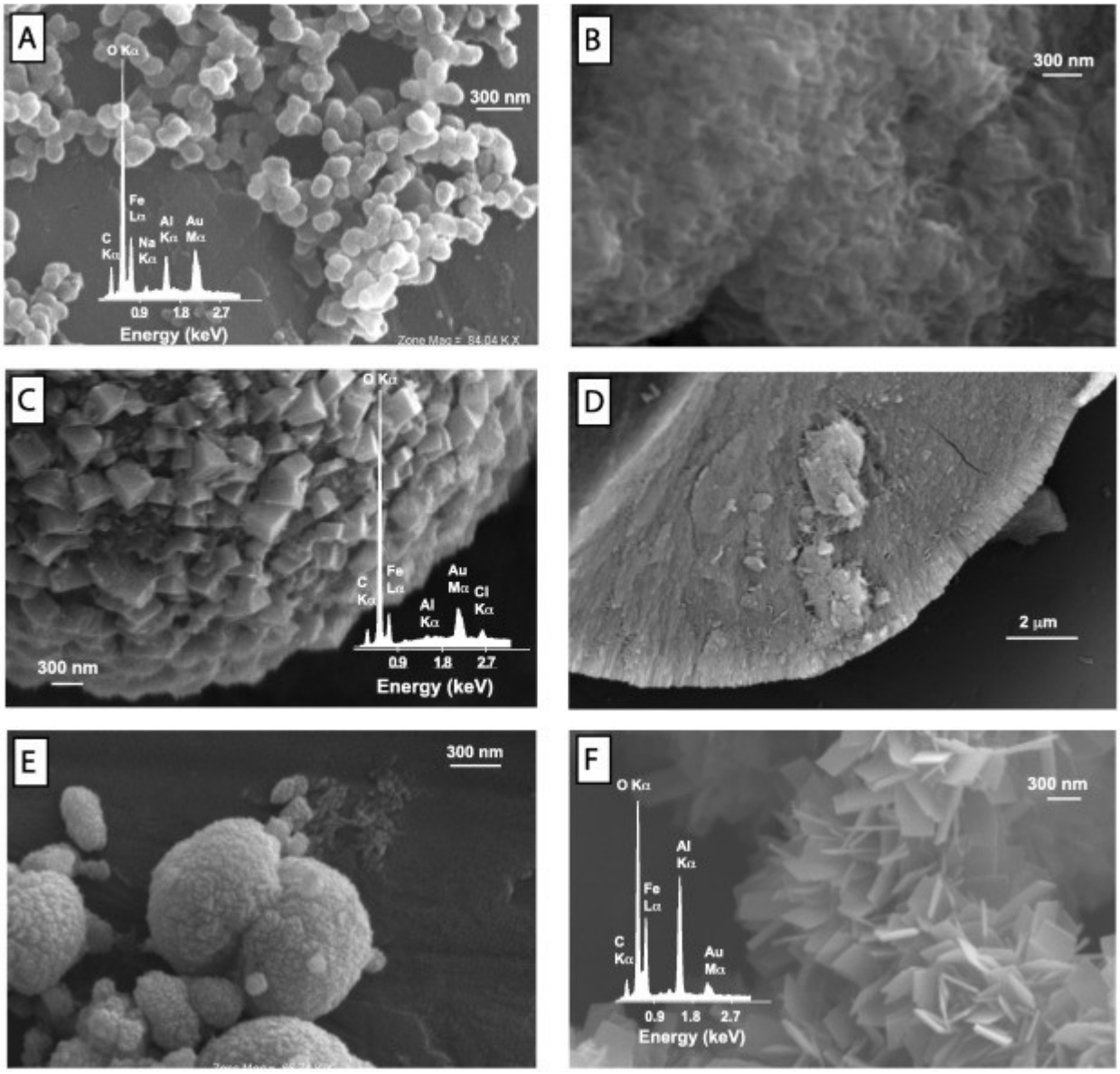

1. Download full-size image

Fig. 2. SEM/EDX of initial precipitates from solutions with (A) 0.1 M $NaHCO_3$, (B) 0.1 M Na_2CO_3 (No EDX), and aged precipitates from solutions with (C) 0.1 M $NaHCO_3$, (D) 0.1 M $NaHCO_3$ that had been crushed (No EDX), (E) 0.1 M Na_2CO_3 (No EDX), (F) 0.1 M Na_2CO_3 and 0.1 M NaOH. Ageing times are similar to those given in Fig. 1.

Ageing of the initial material formed in $NaHCO_3$ solutions resulted in siderite (Fig. 1D). SEM images of this material showed ~10 μm spheres covered with 100–300 nm rhombohedral crystal (Fig. 2C). Images of gently crushed spheres showed that they are composed of an inner region where crystals are so small that their morphology cannot be identified with SEM. However, the outer region is clearly composed of radiating crystal columns (Fig. 2D), consistent with formation through spherulitic growth. Aged precipitates in Na_2CO_3 solutions consisted of siderite together with small amounts of chukanovite (Fig. 1E). SEM images of the material showed rounded to semi-spherical particles (Fig. 2E). These lacked the larger covering crystals observed in $NaHCO_3$ solutions, but were often intergrown. The material formed and aged in a mixture of equimolar Na_2CO_3 and NaOH had broad XRD peaks with positions typical for chukanovite (Fig. 1F). The material was in the form of spheres

built up of plate-shaped crystals, ~30 nm thick (Fig. 2F). Where measured, EDX of both initial and aged material showed peaks from Fe, C, and O, in addition to Au from the coating, Al from the sample holder as well as small amounts of Na or Cl from synthesis solution (Fig. 2). Notably, the initial precipitate contained no detectable Cl, showing that it is not simply hibbingite ($Fe_2(OH)_3Cl$), but rather a Fe-carbonate or -hydroxycarbonate.

TEM images of the initial material formed in $NaHCO_3$ solutions displayed 50–100 nm particles, with selected area electron diffraction rings at $d \approx 2.2$ and 2.6 Å (Fig. 3). With measurement time, the particles developed domains with lattice fringes, suggesting that the initial material was altered when exposed to the electron beam. Similar behaviour has been observed for ACC by Rodriguez-Blanco et al. (2008), and this was attributed to the dehydration and restructuring into a more stable $CaCO_3$ phase. A similar process likely occurred for the Fe-carbonate precipitate.

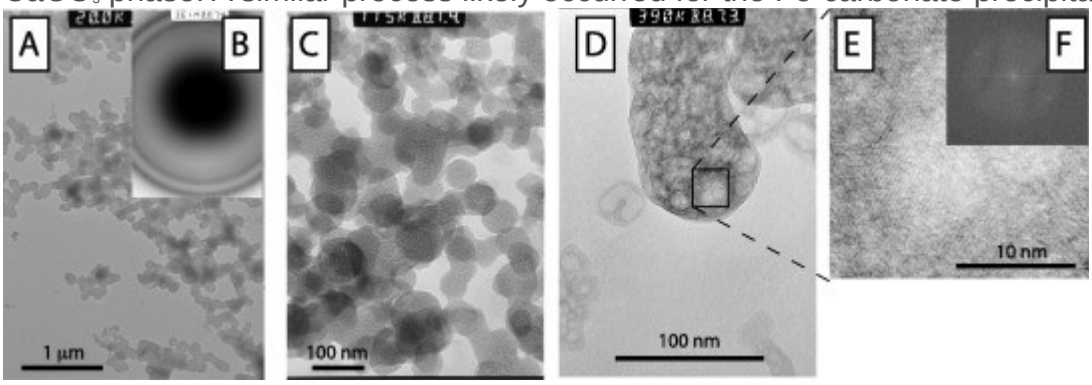

1. Download full-size image

Fig. 3. TEM of initial precipitates from solutions of 0.1 M $NaHCO_3$. (A) Overview image at 20 k magnification with (B) selected area electron diffraction showing rings at d = 2.2 and 2.6 Å. (C) 175 kX image. (D) 390 kX image showing regions with lattice fringes (zoom in (E)) with d = 3 Å in Fourier transforms (F).

To probe the composition of the material, X-ray photoelectron spectroscopy (XPS) was conducted on dried samples. Structural water is expected to degas significantly in the ultra high vacuum of the XPS, but charged species, such as hydroxyl groups, would remain with the solid to greater extent. Fig. 4shows the C1s, O1s and Fe2p spectra for the initial precipitate prepared with $NaHCO_3$. The largest peak in the C1s region represents carbon in carbonate (Stipp and Hochella, 1991, Heuer and Stubbins, 1999, Duckworth and Martin, 2004, Ithurbide et al., 2009). In addition to the peak from carbonate, the C1s region shows two lower binding energy peaks that have contributions from adventitious carbon (the 285 eV peak used for normalisation). The dominant peak in the O1s region at a binding energy of 532.3 can have contributions from oxygen in carbonate (Stipp and Hochella, 1991, Heuer and Stubbins, 1999, Duckworth and Martin, 2004, Ithurbide et al., 2009) as well as in hydroxyl groups (e.g., Rakovan et al., 1999). In addition, the lower binding energy side of the main peak has a clear shoulder, representing a second peak with a binding energy of about 530.6 eV. This peak probably represents oxygen in Fe-(hydr)oxides (e.g., Rakovan et al., 1999, Grosvenor et al., 2004), indicative of slight oxidation. Table 1 shows measured peak positions and areas for all samples. The contributions of carbonate and hydroxyl groups are convoluted in the main O1s peaks at a binding energy of ~532 and cannot be fitted individually. However, based on the values given in

the literature, we would expect the binding energy for O1s in hydroxyl to be somewhat smaller than the value for carbonate (e.g., Stipp and Hochella, 1991, Rakovan et al., 1999, Duckworth and Martin, 2004, Grosvenor et al., 2004), meaning that the main O1s peak should shift to lower binding energy for phases rich in hydroxyl. Furthermore, the intensity of this peak normalised to the intensity of the C1s for carbonate allowed us to probe the hydroxyl/carbonate ratio. Fig. 4 plots the intensity ratio for the samples as a function of the main O1s peak binding energy. Chukanovite has a much higher O/C intensity ratio than siderite as well as a lower O1s binding energy, reflecting structural hydroxide. Compared to siderite, the initial precipitates also have slightly elevated O/C intensity ratios, suggesting that the material could contain some hydroxyl. Based on the assumption that the two highly crystalline phases have compositions according to their published structures, we estimate a dehydrated composition of $Fe(CO_3)_{0.85}(OH)_{0.3}$ for initial precipitates with $NaHCO_3$ and $Fe(CO_3)_{0.7}(OH)_{0.6}$, with Na_2CO_3. However, both of the initial precipitates have an O1s peak representing O in Fe-oxides, showing that oxidation had occurred. Phases such as green rust, ferrihydrite and/or goethite are thus likely to have formed, all of which contain hydroxide, but no or very little CO_3 (Cornell and Schwertmann, 2003). Thus, the actual OH/CO_3 ratio in the initial precipitates is likely to be lower than that estimated. Regardless, the amount of hydroxyl in the material precipitated with $NaHCO_3$cannot account for the weight loss determined for similar material with thermogravimetric analyses (Sel et al., 2012), indicating that the material also contains water, either as a part of its structure or as an adsorbed species.

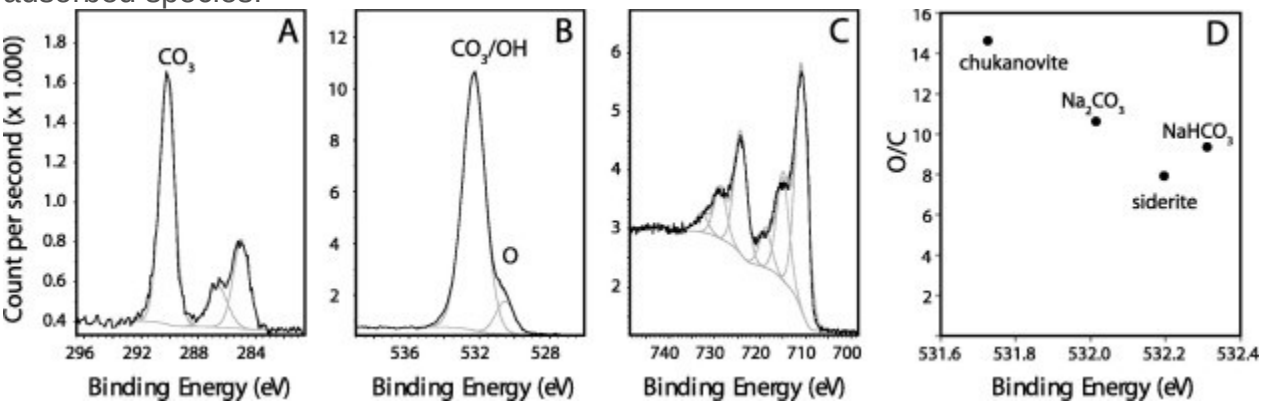

1. Download full-size image

Fig. 4. XPS example of the (A) C1s region, (B) O1s region and (C) Fe2p region for an initial precipitate made using $NaHCO_3$. Peak positions have been calibrated assuming adventitious carbon at a binding energy of 285 eV. (D) Shows the O/C area ratio for the material as a function of the binding energy of the main O1s CO_3/OH peak.

Table 1. XPS peak position, full width at half maximum (FWHM) and area for siderite (from $NaHCO_3$), chukanovite (from equimolar Na_2CO_3/NaOH mixture) and initial precipitates formed in $NaHCO_3$ or Na_2CO_3. Peak positions have been calibrated so that the C1s binding energy for adventitious carbon equals 285 eV. For Fe2p, the binding energy and FWHM refer to the first Fe2p 3/2 peak, whereas the area represents all Fe2p peaks.

	Element	**C1s**	**O1s**		**Fe2p**
Material	**Component**	**CO_3**	**CO_3 and OH**	**O**	
Siderite	Binding energy (eV)	290.0	532.2		710.7

	Element	C1s	O1s		Fe2p
Material	**Component**	**CO_3**	**CO_3 and OH**	**O**	
	FWHM (eV)	1.2	1.5		3.2
	Area	3051	24,177		33,602
Chukanovite	Binding energy (eV)	289.8	531.7	529.9	710.5
	FWHM	1.3	1.5	1.3	3.2
	Area	1067	15,607	3835	38,500
Na_2CO_3	Binding energy (eV)	289.9	532.0	530.2	710.4
	FWHM	1.4	1.5	1.3	3.1
	Area	2376	25,262	1475	49,031
$NaHCO_3$	Binding energy (eV)	290.2	532.3	530.5	710.9
	FWHM	1.2	1.5	1.3	3.2
	Area	4162	38,960	4210	78,741

Fig. 5 shows the X-ray diffraction patterns for precipitates obtained from synchrotron X-ray scattering (given as I(*Q*)). The initial precipitates formed in $NaHCO_3$ and Na_2CO_3 solutions show broad peaks at Q-values of 1.3, 2.4 and 6.2 $Å^{-1}$, and a broad shoulder at 3.8 $Å^{-1}$ (Table 2). I(*Q*) of aged material shows Bragg reflections consistent with siderite ($NaHCO_3$ experiments), chukanovite (experiments with equimolar Na_2CO_3 and NaOH) and $Fe(OH)_2$(experiments with NaOH).

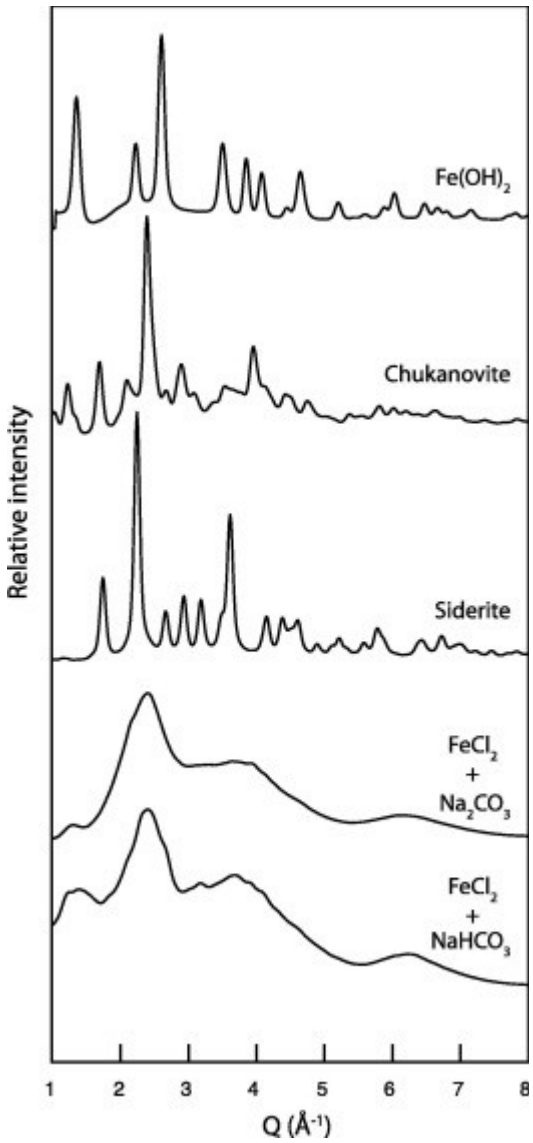

1. Download full-size image

Fig. 5. I(*Q*) for initial precipitates as well as synthesised Fe-carbonates and hydroxides. Except for $Fe(OH)_2$, the materials were dried before analysis. The *d*-spacing for peaks are given in Table 2.

Table 2. Peak positions in the I(*Q*) and the G(*r*). Values are given as *Q* and as the traditional *d*-spacing.

Sampling type	**Initial**	**Initial**	**Aged**	**Aged**	**Aged**
Carbonate solution	0.1 M $NaHCO_3$	0.1 M Na_2CO_3	0.1 M $NaHCO_3$	0.1 M Na_2CO_3	–
Base	–	–	–	0.1 M NaOH	0.2 M NaOH
Sample preparation	Dried	Dried	Dried	Dried	Wet
I(*Q*) peak positions (*Q*; $Å^{-1}$)	1.3	1.3	1.73	1.21	1.35
	2.2	–	2.23	1.68	2.21
	2.4	2.4	2.65	2.11	2.6
	3.8	3.8	2.92	2.38	3.5

Sampling type	Initial	Initial	Aged	Aged	Aged
	6.2	6.2	3.18	2.88	3.84
			3.6	3.65	4.08
			4.13	3.95	4.65
I(*Q*) peak positions (*d*; Å)	4.83	4.83	3.63	5.19	4.65
	2.85	–	2.82	3.74	2.84
	2.62	2.62	2.37	2.98	2.42
	1.65	1.65	2.15	2.64	1.79
	1.01	1.01	1.97	2.18	1.64
			1.74	1.72	1.54
			1.52	1.59	1.35
G(*r*) peak positions (Å)	1.3	1.3	1.3	1.3	
	2.12	2.12	2.14	2.13	2.13
			3.02		2.81
	3.18	3.20	3.24	3.25	3.26
			3.73		3.95
	4.20	4.22	4.07	4.32	
			4.64	5.00	5.09
	5.42	5.42	5.87	5.70	5.64
	6.26	6.26	6.65	6.55	7.32
					8.63

The initial precipitates from $NaHCO_3$ and Na_2CO_3 solutions have reduced pair distribution functions, G(*r*), with peaks occurring at very similar *r*-values (Fig. 6; Table 2): a weak and poorly resolved peak at $r = 1.3$ Å (peaks labelled in Fig. 6 in the order mentioned here), representing C–O distances in carbonate, and stronger peaks at $r = 2.12$ Å (representing largely Fe(II)–O), $r \approx 3.19$ Å and $r \approx 4.21$ Å, as well as weaker peaks at $r \approx 5.42$ Å and $r \approx 6.26$ Å. Measurement of the sample prepared using vacuum filtration yielded a PDF essentially identical to those obtained for material produced using centrifuge filtration. The *r*-values for the C–O peak and the first Fe(II)–O peak are comparable in all carbonate precipitates, reflecting the structure of the carbonate group and the ionic radii of high spin Fe(II) when octahedrally coordinated with O. The width of the Fe(II)–O peak for chukanovite (FWHM of ~2.29 Å) is slightly larger than for siderite (FWHM of ~2.25 Å), reflecting its distorted octahedra with Fe–O distances of 2.01–2.47 Å (Pekov et al., 2007). The Fe(II)–O peak width for the initial precipitates is comparable to that of chukanovite, suggesting that the materials have distorted octahedra or variable Fe coordination environments. The position of the first peak, representing Fe–Fe distance, depends on the type of sharing of the Fe octahedra. Treating the Fe and O as hard spheres separated by a distance of 2.12 Å, geometric calculations of Fe–Fe distance for undistorted octahedra yielded $4.24 \text{ Å} \leqslant r < 3.00 \text{ Å}$ for corner sharing, $3.00 \text{ Å} \leqslant r < 2.46 \text{ Å}$ for edge sharing

and r = 2.46 Å for face sharing. Based on published structures (Graf, 1961, Pekov et al., 2007), calculated interatomic distances between specific elements with PDFgui yield Fe-Fe distances of ~3.72 Å for the corner sharing octahedra in siderite. For chukanovite, edge sharing octahedra have average distances of ~3.25 Å because of their distortion. This means that the position of the Fe–Fe peak coincides with a minor O–O peak that contributes about 15% of the total peak intensity. The strong peak at ~3.19 Å for the initial precipitates suggests that they also have a large proportion of distorted edge sharing Fe octahedra and/or corner sharing octahedra. Apart from the stronger peaks that can be largely attributed to specific element pairs, the initial precipitates have peaks at r-values of ~4.21, 5.42 and 6.26 Å (labelled 4–6 in Fig. 6), whose intensities have contributions from several pairs. These interatomic distances do not exist in any of the aged phases and the PDF for the initial precipitates cannot be fit with PDFgui with a combination of the structures for the crystalline phases. Thus, the initial precipitates differ in structure from known Fe(II)-carbonate and hydroxides.

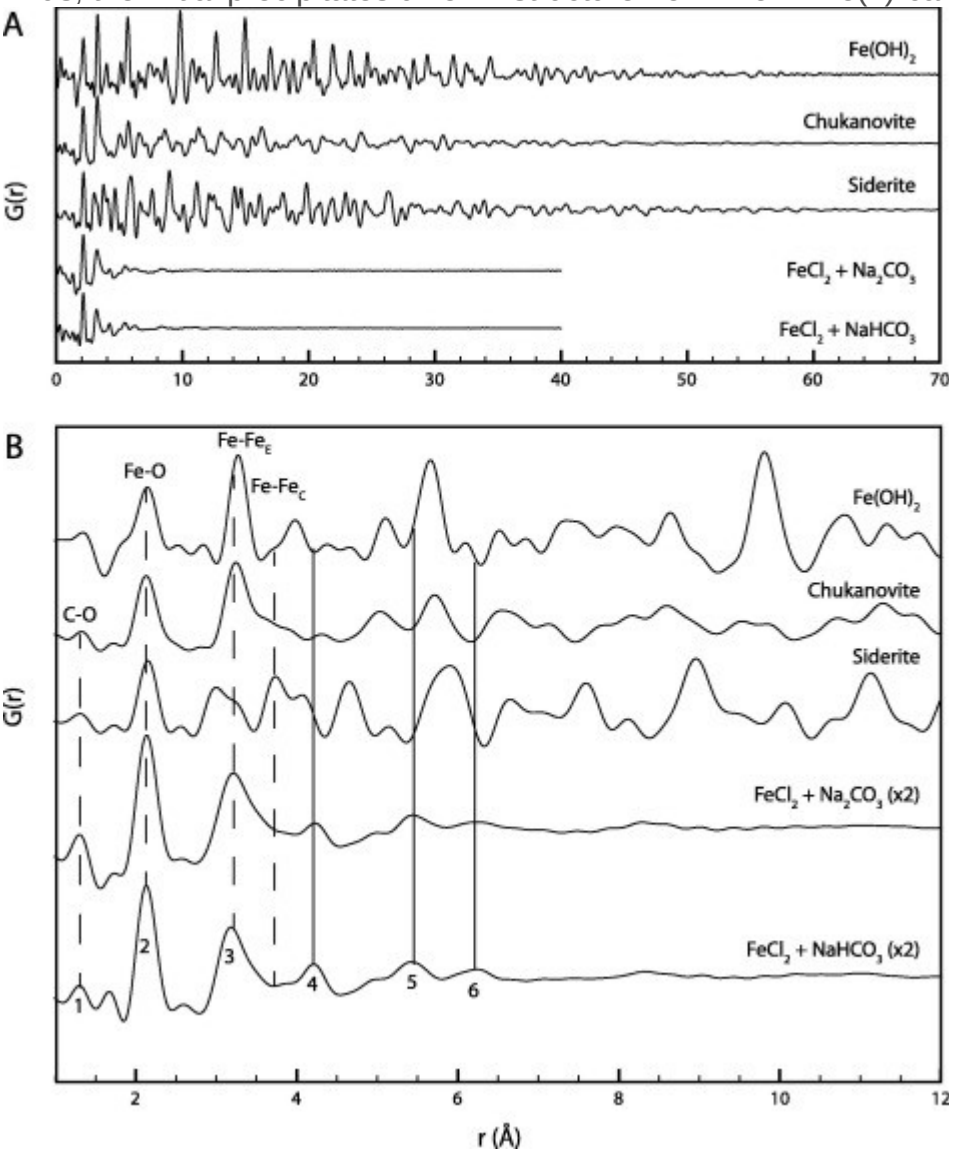

1. Download full-size image

Fig. 6. (A) Overview of the G(r) for initial precipitates as well as synthesised Fe-carbonates and hydroxides. The G(r) decays quickly with increasing r-values for the initial material, reflecting smaller coherently scattering domains. (B) Zoom of region with lower r-values. Peak intensities of the initial

precipitates have been doubled (marked “x2”), so that the smaller peaks at $r > 4$ Å are discernable. Dashed lines indicate position of from atomic pairs of C–O, Fe(II)–O and Fe(II)–Fe(II) in edge and corner sharing octahedra (subscript E and S), whereas solid lines refer to peaks in the initial precipitate that does not appear in the aged materials. Except for $Fe(OH)_2$, the materials were dried before analysis.

Mössbauer spectroscopy of the initial and aged materials also suggests that the initial material is less crystalline than the aged material (Fig. 7; Table 3). The initial materials show a double absorption line (a doublet) at all measured temperatures, whereas siderite and chukanovite display several absorption lines at lower temperature, reflecting magnetic ordering (e.g., Forester and Koon, 1969). Moreover, the line width of the initial material is slightly larger than those of the aged materials at all measured temperatures. At 40 K, all spectra display two absorption lines from a doublet and the isomer shift, δ, for all of the materials is similar. However, the quadrupole splitting, Δ, of the initial material is significantly larger than those for siderite and chukanovite, consistent with differences in local structure. The quadrupole splitting in Mössbauer spectra arises from the Coulomb interaction of an aspherical nucleus with the electric field gradient from the surrounding charges. Changes in the electric field gradient can be a result of changes in the symmetry of the coordination polyhedra. Chukanovite, for example, has distorted polyhedra and displays larger Δ than siderite. We propose that the increased Δ-value for the initial material compared to chukanovite and siderite is the result of more distorted octahedra due to lacking long-range crystalline order and possibly also coordination of a ligand other than CO_3^{2-} to the central Fe(II), e.g., water or hydroxyl.

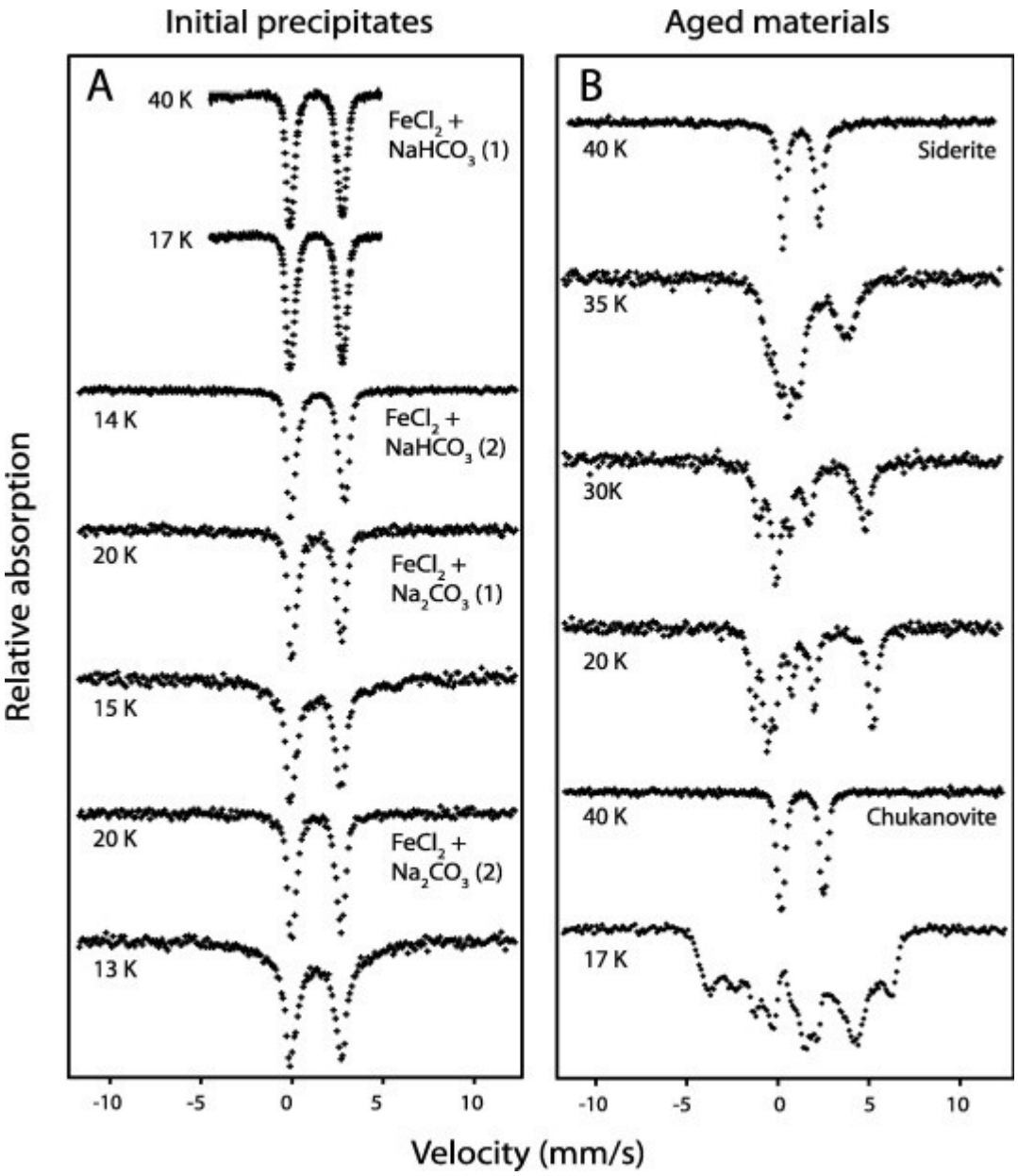

1. Download full-size image

Fig. 7. Mössbauer spectra obtained at low temperatures of initial and aged materials. (A) Initial precipitates from 0.1 M $FeCl_2$ and 0.1 M $NaHCO_3$ as well as 0.1 M $FeCl_2$ and 0.1 M Na_2CO_3. (B) Siderite and chukanovite. Sample $FeCl_2$ + $NaHCO_3$ (1) was resuspended in water before preparation and freezing in liquid nitrogen to minimise the contribution from dissolved Fe.

Table 3. Fitted Mössbauer parameters for doublets.

Sample	Temperature (K)	δ (mm/s)	Δ (mm/s)	Line width (mm/s)
Aged materials				
Siderite	40	1.35	2.04	0.46
Chukanovite	40	1.3	2.35	0.46
Initial precipitates				
$FeCl_2$ + $NaHCO_3$ (1)	40	1.33	2.84	0.53
Resuspended in water	17	1.34	2.85	0.54

Sample	Temperature (K)	δ (mm/s)	Δ (mm/s)	Line width (mm/s)
$FeCl_2$ + $NaHCO_3$ (2)	14	1.36	2.93	0.54
$FeCl_2$ + Na_2CO_3 (1)	20	1.30	2.70	0.54
	13	1.33	2.75	–*
$FeCl_2$ + Na_2CO_3 (2)	20	1.31	2.70	0.57
	15	1.31	2.72	–*

*Line widths poorly defined because of broadening.

In the G(*r*) of the initial material (Fig. 6), the peak intensities decrease rapidly with increasing interatomic distance for the initial precipitates, demonstrating a lack of long range ordering that could reflect an amorphous solid. However, peaks at $r \geqslant 3.19$ Å in the G(*r*) are well defined compared to ACC, and those at 10–15 Å are more intense (Michel et al., 2008, Radha et al., 2012). Thus, coherent scattering domains appear slightly larger for the initial iron carbonate precipitates, and atomic positions are more defined, meaning that we cannot fully exclude the possibility that the material is nanocrystalline rather than truly amorphous.

Molecular dynamics simulations were performed to probe the structural evolution of the earliest formed Fe(II) carbonate clusters from highly concentrated solutions following the methodology of Wallace et al. (2013). The results indicate that polynuclear complexes are favoured to form in solution. The structures of the polynuclear complexes are highly dynamic, as observed in simulations of calcium carbonate clustering (Demichelis et al., 2011, Wallace et al., 2013). Interestingly, the time averaged radial distribution function for the polynuclear complexes (clusters) agrees qualitatively with the first 6–8 Å of the PDF measured here for the initial precipitates (Fig. 8). Thus, the initial precipitates carry the structural motif predicted for polynuclear complexes. We propose that the initial precipitates are condensates of polynuclear complexes of variable structure, assembled in a relatively unorganised fashion that only gives rise to order on the scale of 15 Å, rather than being composed of discrete nanocrystals with a well-defined structure.

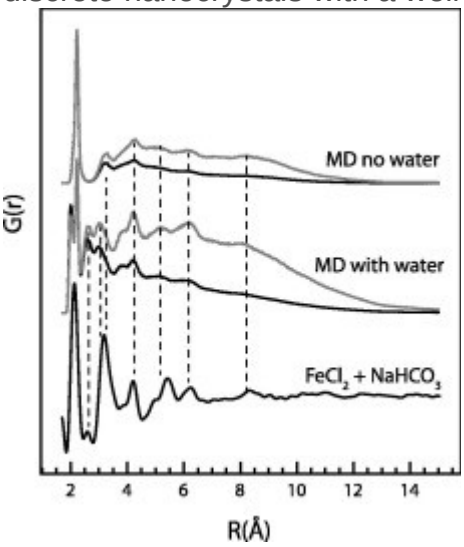

1. Download full-size image

Fig. 8. Comparison of the measured PDF for the initial material with the average radial distribution function of polynuclear Fe-carbonate complexes from molecular dynamics (MD; including and

excluding the contributions to the function from oxygen atoms in coordinating water molecules). For the grey curves, the G(*r*) has been multiplied with *R*to more clearly visualise the position of smaller peaks at higher *R*-values. Doted lines highlight the peaks in the MD radial distribution functions. Note that the measured PDF is a *reduced* pair distribution function, that oscillates around 0. In contrast, the radial distribution functions derived from molecular dynamics oscillate between 0 and 1 and do not include the effect of variable element specific scattering.

To probe the structure of the crystalline phases at the local scale, structural models of siderite and chukanovite (Graf, 1961, Pekov et al., 2007) were fitted to their PDFs using the software PDFgui (Farrow et al., 2007), the “real” space counterpart of Rietveld refinement. The fit of siderite (Fig. 9A) agrees well with the experimental data and resulted in reasonable parameters (a = 4.71 Å, c = 15.42 Å, δ_2 = 3.5, U_{Fe} = 0.008 Å^2, U_C = 0.015 Å^2, U_O = 0.019 Å^2; Fe occupancy: 1.0; Rw: 0.205) and a coherent scattering domain size, ∼250 Å, which is above the value that can be confidently estimated because of instrumental contribution to peak decay (∼80 Å). Allowing the Fe occupancy to vary resulted in a value of 1.03, but this fitting did not significantly decrease the residual. For chukanovite, the fit is somewhat poorer (Fig. 9B) and the determined parameters (a = 12.34 Å, b = 9.38 Å, c = 3.21 Å, δ_2 = 3.5, U_{Fe} = 0.011 Å^2, U_C = 0.026 Å^2, U_O = 0.020 Å^2; domain size of ∼100 Å: Rw: 0.321) showed a larger isotropic displacement factor for carbon than for oxygen, which is unreasonable given that the C resides inside a relatively rigid carbonate group. Fitting the Fe occupancy resulted in a value of 1.07 for Fe1 and 0.93 for Fe2, but did not significantly improve the quality of the fit. Although many peaks are fit adequately, agreement with the first three intense peaks is poor.

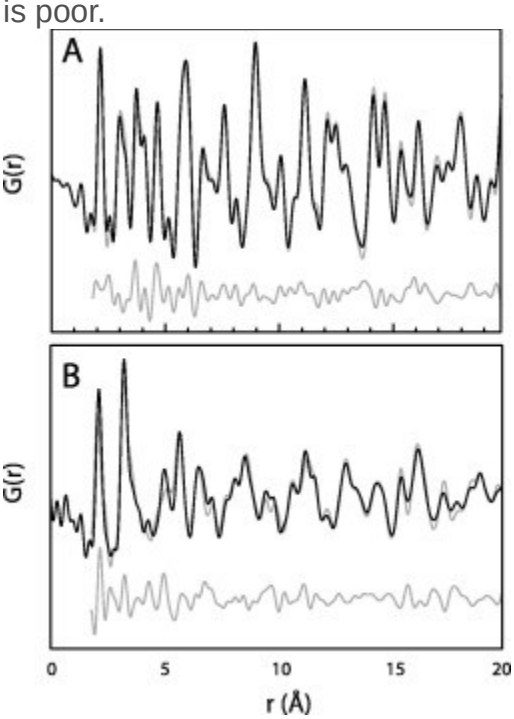

1. Download full-size image

Fig. 9. PDFgui fitting of dried (A) siderite and (B) Chukanovite. The black curve represents the experimental data, the grey curve portraits the fit and the curve at the bottom provides the residual.

The discrepancies could be the result of $Fe(OH)_2$ impurities. The I(*Q*) of chukanovite shows no evidence of the presence of such a phase, but $Fe(OH)_2$ could have formed as a nanocrystalline material, broadening its Bragg peaks. In the PDF, $Fe(OH)_2$ features strong peaks at 2.12 and 3.26 Å as well as a weaker peak at 5.08 Å (Fig. 6), where the calculated pattern indeed underestimates the observed peak intensities. However, the pattern for $Fe(OH)_2$ also has a weaker peak at 3.94 Å and very intense peaks at 5.6 and 9.8 Å. At these *r*-values, the calculated pattern leaves little or no room for contributions to intensity from $Fe(OH)_2$, suggesting that it is not present in detectable amounts. To further probe for the presence of $Fe(OH)_2$, the pattern was fitted with both the chukanovite and $Fe(OH)_2$ structure. This fitting indicated the presence of 5% $Fe(OH)_2$ with very small coherent scattering domains of 10 Å. However, the inclusion of $Fe(OH)_2$ in the fit did not yield significant improvement (Rw improved from 0.321 to 0.314), indicating that the amount of $Fe(OH)_2$ in the sample is lower than what can be confidently detected with PDF. Important to this discussion is the fact that including the phase as a fit parameter did little to resolve the discrepancies between the measured and calculated pattern, suggesting that slight inconsistencies exist between the structural model derived from traditional XRD and the local order of the chukanovite produced here. The first clear peak, representing dominantly Fe–O, is shifted to higher *r*-values than expected from the structure and does not have a clear shoulder. Similarly, the second, most intense peak, representing mainly Fe–Fe, features a weaker shoulder at higher r-value than predicted from the structure. The lack of shoulders could reflect that some Fe octahedra are less distorted in the material synthesised here. Alternatively, some of the more distorted Fe sites in the structure could be vacant, decreasing their signature in the PDF. However, a fitting of occupancy does not clearly suggest this.

3.2. In-situ characterisation of transformation

The first, preliminary experiments to characterise the local structure of the initial precipitate from $NaHCO_3$ solutions were carried out with dried solids in sealed capillary tubes of Kapton, a material regularly used as a sample holder for Fe(II)-bearing solids to minimise oxidation. However, this preparation method repeatedly resulted in pervasive oxidation before analysis. In one experiment, the loaded tube was plunged into liquid nitrogen to minimise oxidation during transport from the anaerobic chamber to the beamline. This sample was whitish upon mounting for X-ray scattering and seals appeared intact. Fig. 10A shows the acquired PDFs as a function of the time elapsed after mounting. The PDF of the first sample measured after 5 min is very similar to one acquired in glass, but showed a slight decrease in the *r*-value of the Fe–O peak to ~2.08 Å (peak 2 on Fig. 10A). As time progressed, the *r*-value of the Fe–O peak decreased to 1.98 Å, the peak at ~3.19 Å (peak 3) broadened and split into two peaks. Finally, peak 4 at ~4.21 Å disappeared and a new peak appeared at $r \approx 4.73$ Å. In the process, peaks at higher *r*-values shifted and increased in intensity, showing that the coherent scattering domains grew in size. The PDF of the end product after 45 min strongly resembles that of a ferrihydrite standard precipitated from rapid hydrolysis of an $FeCl_3$ solution (bottom PDF in Fig. 10A), showing that the initial material oxidises when measured in Kapton containers (but not in glass capillary tubes).

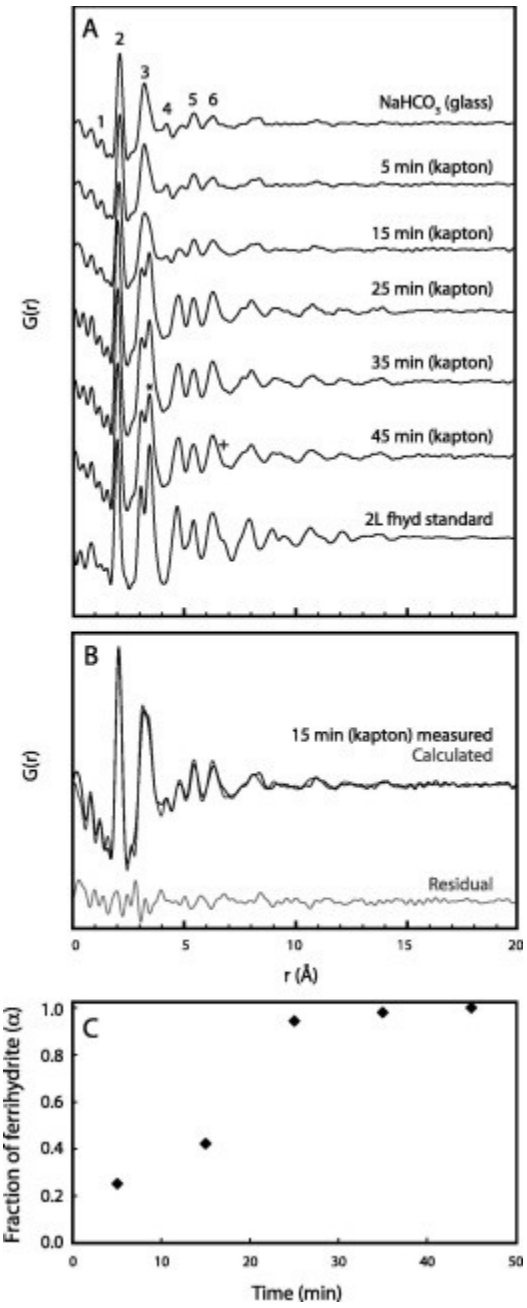

1. Download full-size image

Fig. 10. (A) PDFs measured for the initial material in a Kapton capillary tube. The loaded tube was transported to the beamline in liquid nitrogen to minimise oxidation. Also shown is a PDF of the initial material in glass and a PDF of a ferrihydrite standard precipitated from rapid hydrolysis of $FeCl_3$. (B) Example of the fitting of the sample measured after 15 min with the deconvolution method. (C) Determined relative proportion of ferrihydrite with the deconvolution method as a function of time.

The end product after 45 min and the ferrihydrite standard show some notable differences: (1) The peaks of the end product decrease more rapidly with increasing *r*-value, meaning that its coherent scattering domains are smaller. (2) The intensities are decreased for the second double peak at $r \approx 3.45$ Å (labelled with * on Fig. 10A) and for the shoulder at $r \approx 6.8$ Å (labelled with + on Fig. 10A). The intensities of these two peaks have been shown to increase with the size of ferrihydrite's coherent scattering domains (Michel et al., 2010). Based on PDFgui fitting and a revised

model for the ferrihydrite structure, the intensity increase has been interpreted to reflect increasing Fe occupancy in the structure as ferrihydrite crystals increase in size (Michel et al., 2007, Michel et al., 2010). The appearance of the PDF pattern acquired here for ferrihydrite with small coherent scattering domains agrees qualitatively with the one predicted from Michel et al. (2010).

To determine the change in the relative proportions of ferrihydrite with time, the PDFs were deconvoluted based on the assumption that the patterns could be described by a combination of two end members: The unoxidised material measured in a glass capillary tube, assumed to be identical to the initial material in the Kapton capillary tube, and the sample measured after 45 min, assumed to represent a pure ferrihydrite end-member. Using Excel with the solver function, a PDF pattern was calculated from linear combination of the end members, which were scaled to minimise the summed square of the residual. The calculated and measured PDF are shown in Fig. 10B for the sample measured after 15 min. The calculated proportions as a function of time (Fig. 10C) indicate that the initial precipitate has essentially oxidised to ferrihydrite after half an hour, despite encapsulation in Kapton, i.e., it is highly sensitive to oxidation by air.

To determine the rate of transformation of the initial precipitate in the solution, slurries of fresh materials precipitated with $NaHCO_3$ only, with an equimolar $NaHCO_3/Na_2CO_3$ mixture and with Na_2CO_3 only, were transferred to glass capillary tubes, sealed and centrifuged. The change in structure of the solids in solution was then determined with high energy XRD and PDF analysis after subtraction of a water background. Fig. 11 displays the evolution of the PDF at various time points for an experiment with $NaHCO_3$. Early PDFs show only the signal of the short range ordered precursor, but with time peaks appear for siderite in experiments with $NaHCO_3$ (after ~1 h) and $NaHCO_3/Na_2CO_3$ (after ~2 h) and for siderite and chukanovite in experiments with Na_2CO_3 (after ~6 h).

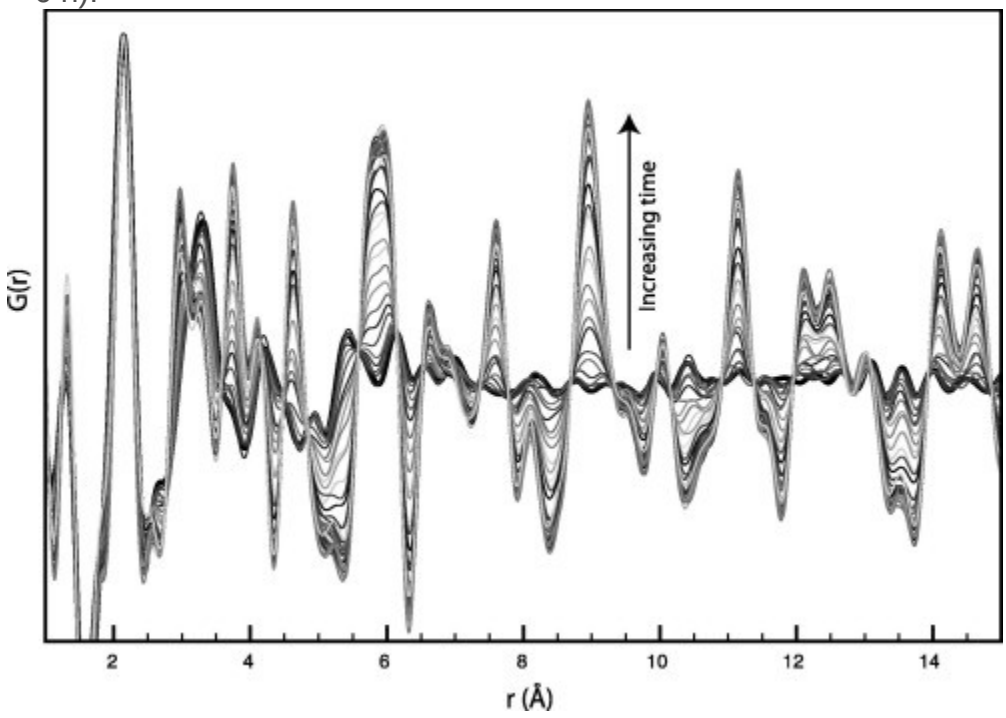

1. Download full-size image

Fig. 11. PDFs of material precipitated in $NaHCO_3$ acquired in the original synthesis solution over time. The signal for the initial precipitate is marked with a thick black line. Within 1 h, peaks grow at the positions expected for siderite (exemplified for one peak only).

To quantify the relative abundance of phases, two methods were employed: (1) the deconvolution calculations used for the oxidation experiment taking the first sample as the end member for the initial material and siderite and chukanovite standards (measured in solution) as the final end members; and (2) fitting with PDFgui. With PDFgui, proper fitting can only be carried out for phases with known structure. To circumvent this problem, siderite and chukanovite scaling was first fitted to the PDFs acquired in solution at *r*-values above 3.8 Å, where the precursor has very little peaks. In this fitting, parameters other than scaling were fixed at the value determined from the fitting of the dried standards. The total amount of siderite, chukanovite and precursor was then determined by fitting the scaling of crystalline phases to the peak at $r \approx 2.12$ Å only, fixing the relative scaling of siderite and chukanovite at the value obtained from the fit with $r > 3.8$ Å. The ~2.12 Å peak represents Fe–O atomic pairs as well as a minor contribution from O–O in carbonate (10% of the Fe–O contribution). In the PDF, peak intensities depend on the scattering power of the atomic pairs in the coordination sphere as well as the coordination number. Thus, this fitting is based on the assumption that Fe is in octahedral coordination in all phases and that the variation in the contributions from O–O atomic pairs in carbonate is negligible. Adding to the uncertainties, inaccuracies arise from inadequate subtraction of the water background, which introduces significant noise in the PDFs, affecting the intensity of ~2.12 Å peak.

The fitted relative proportion of siderite and chukanovite as a function of time at different synthesis conditions is shown in Fig. 12. The fitted proportions show a relatively well-defined trend that agrees qualitatively with the growth of Bragg peaks in the diffraction data. Except for the sample precipitated with Na_2CO_3, the relative proportion determined with the two methods agree well. However, for many experiments the proportion of crystalline phases fitted with PDFgui does not reach 1; this is especially clear for the experiment with Na_2CO_3 (Fig. 12C). Although this might reflect the presence of a small amount of residual precursor, it could also reflect systematic errors introduced into the PDF because of inadequate background correction that results in an increased intensity in the Fe–O peak compared to other peaks. For the experiment with Na_2CO_3, the inadequate fitting of chukanovite also contributes. Regardless, the data show that most of the precursor phase transformed within 12 h.

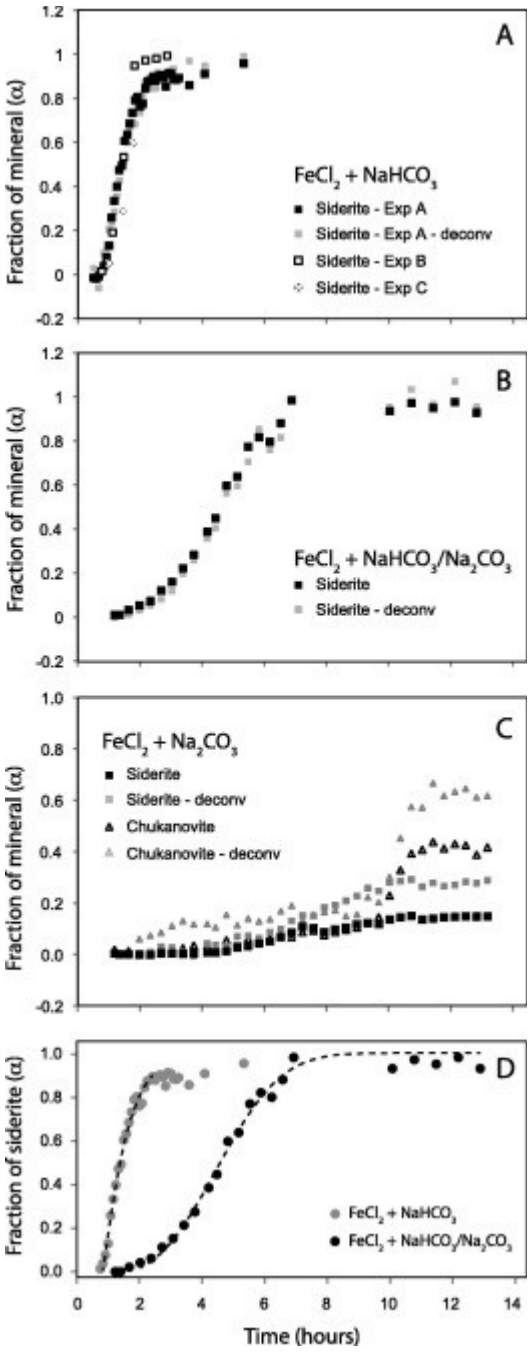

1. Download full-size image

Fig. 12. Relative proportions of siderite and chukanovite as a function of time for experiments with $FeCl_2$ and (A) $NaHCO_3$, (B) $NaHCO_3/Na_2CO_3$ mixtures, and (C) Na_2CO_3. Black symbols represent proportions derived from PDFgui fitting, whereas grey symbols represent those from the deconvolution. (D) Fit of the siderite proportions determined with PDFgui using the JMAK equation (Eq. (1)) for experiments with $FeCl_2$and $NaHCO_3$ as well as with $FeCl_2$ and $NaHCO_3/Na_2CO_3$ mixtures.

In experiments with only one transformation product, the proportion of this phase can be fitted with the Johnson–Mehl-Avrami-Kolmogorov (JMAK) equation, providing information on the transformation kinetics, nucleation rate and the growth mechanism (e.g., Yee et al., 2006):

$$\alpha = 1 - e^{-k(t-t_0)^m} \quad (1)$$

where t is time in hours, t_0, the induction time, k, the reaction constant and m, the Avrami exponent. The exact physical meaning of the Avrami exponent is debated (e.g., Clavaguera-Mora et al., 2002), but it is agreed that it encompasses a parameter describing the dimensionality of growth. Often, the Avrami exponent is held to be composed of three parameters (e.g., Hulbert, 1969, Starink, 2001, Kooi, 2006):

$$m = N_{dim} g + B \quad (2)$$

Here, N_{dim} is the dimensionality of the growth (e.g., 1 for linear growth) and $g$depends on the nature of the process that is rate limiting for mass transfer (also termed boundary conditions), taking the value 1 for surface-controlled reaction and 1/2 for diffusion-controlled reaction. The parameter B relates to the rate of nucleation of the new-formed phase, based on the assumption that the number of nuclei at time t, $N(t)$, is related to the initial number of nuclei $N_0$by simple power law:

$$N(t) = N_0\, t^B, \quad (3)$$

taking a value of 0 if all nuclei are present initially and 1 if nuclei are formed at a constant rate. Fig. 12D shows fit of the proportions of siderite determined with PDFgui to the JMAK equation. The derived parameters are t_0 = 0.8 h, k = 1.4 h^{-1} and m = 1.2 for the material formed in $NaHCO_3$ and t_0 = 0.8 h, k = 0.02 h^{-1} and m = 2.8 for the material formed in $NaHCO_3$/Na_2CO_3 mixtures. The large difference in m suggests that siderite crystal growth differs in the two experiments. m = 2.8 determined for siderite formed from the mixture agrees relatively well with two- or three-dimensional growth of siderite, whereas m = 1.2 could represent one-dimensional growth, similar to that predicted from SEM images of siderite columns in the outer region of the spheres (Fig. 2D). Alternatively, the change in m from 2.8 to 1.2 might reflect a transition from a surface-controlled to diffusion-controlled reaction with decreasing pH, similar to what is observed for calcite dissolution (Sjöberg and Rickard, 1984).

4. Implications

Metastable precursors decrease the activation energy that must be overcome during nucleation. This makes precipitation of a secondary phase more likely (e.g., Steefel and Van Cappellen, 1990). In recent in-situ TEM images of the transformation of ACC, for example, identified nucleation points are close to the disordered precursor's surface (Nielsen et al., 2014). Thus, the existence of an iron carbonate precursor may facilitate formation of siderite and chukanovite, for example through its heterogeneous nucleation on the precursor surfaces and/or by providing an environment of high ion mobility as proposed by Nielsen et al. (2014).

Our results indicate that several aspects greatly complicate identification of the iron carbonate precursor: (1) It transforms quickly in solution (at least for the pure system), with a lifetime of about 3 h at circumneutral pH. (2) It is highly reactive towards oxidation by air. (3) It produces no clear Bragg peaks in XRD. It is therefore a possibility that the material could very easily have gone undetected in previous studies. Circumstantial evidence suggests that it might form in laboratory experiments and during corrosion. For example, in recent experiments with dissimilatory iron reducting bacteria, 20–200 nm iron carbonate spheres developed, which displayed a Raman band at

1039 cm^{-1}that the authors attributed to either an unknown/amorphous form of carbonate or to C–C vibrations in organic material (Sánchez-Román et al., 2014). Upon 45 days of ageing, the authors observed larger spherulites. Furthermore, siderite formed in the laboratory through degassing of CO_2 shows the same morphology as our material aged in $NaHCO_3$ (Wiesli et al., 2004), and siderite formed in the early stages of other dissimilatory iron reduction experiments has morphologies resembling that of our material aged with Na_2CO_3 (Johnson et al., 2005), indicating the possibility that these experiment also formed siderite from precursors.
During CO_2 sequestration, the iron carbonate precursor could form if dissolved CO_2 leaks from storage formations. Finally, during corrosion of Fe^0, X-ray amorphous iron carbonate has been proposed to form based on significant loss of carbonate from solution in column experiments, as well as the lack of peaks from crystalline iron carbonate in XRD (Gu et al., 1999). This material might be the short ranged ordered Fe-carbonate identified here. If so, it is likely to form during anaerobic corrosion of infrastructure used in CO_2 sequestration.

5. Conclusions

Rapid precipitation of iron carbonate results in material with no long-range order over a relative wide pH range. Based on XPS measurement, the material contains Fe, carbonate and possibly smaller amounts of hydroxyl. PDF analysis of high energy X-ray scattering data as well as Mössbauer spectroscopy show that the material differs in structure from known Fe-carbonates and hydroxides. The size of the coherent scattering domains is consistent with the material being nanocrystalline and not truly amorphous. Measured PDFs qualitatively agree with those determined from molecular dynamics modelling of an ensemble of polynuclear Fe-carbonate complexes. This offers the possibility that the material is a condensate of polynuclear complexes, assembled in a largely unorganised fashion to produce coherent scattering domains of a size of ∼15 Å, rather than being composed of discrete nanocrystals with a well-defined structure.

PDF measurements as a function of time show that the short ranged ordered material oxidises readily, transforming to ferrihydrite within half an hour when encapsulated in Kapton. Measurements performed on material in solution inside glass capillary tubes show that the short ranged ordered precipitate can transform to siderite and chukanovite. The reaction proceeds faster at lower pH, with transformation being complete after ∼3 h at circumneutral pH. In natural settings, the identified precursor is likely to form where Fe(II) and carbonate concentrations are high, for example during anaerobic corrosion or bacterial Fe reduction.

Acknowledgements

We warmly acknowledge Alejandro Fernandez-Martinez for introduction to the PDF technique and many stimulating discussions and we are grateful for the kind help given by Nancy Lazarz and Joanne Stubbs, GeoSoilEnviroCARS, University of Chicago, and Mark Vukonich, BioCAT; The Banfield group and Tim Teague, U.C. Berkeley; Susan Stipp, Keld West, Juan Diego Rodriguez-Blanco, Henning Osholm Sørensen and Erik Johnsen, University of Copenhagen; A.V. Radha, U.C.

Davis; Helge Rasmussen, DTU; Karina Chapman, Peter Chupas, Rick Spence and Kevin A. Beyer, APS beamline 11 ID-B. We thank the CarbFix team for discussions and encouragement, and Sirine Fakra, Advanced Light Source, for trying X-ray absorption spectroscopy. Tonci Balic-Zunic from the Natural History Museum of Denmark for kindly providing siderite and magnetite crystals.

This work was funded by the Villum Kann Rasmussen Foundation; The European Community through funding of the CarbFix project, Grant Agreement No. FP7-283148; The Danish Councils for Independent Research(Via DANSCATT) for funding travel costs; The project was partially supported by the Center for Nanoscale Control of Geologic CO_2, an Energy Frontier Research Center funded by the U.S. Department of Energy, Office of Science, Office of Basic Energy Sciences under Award No. DE-AC02-05CH11231. This research used resources of the Advanced Photon Source, a U.S. Department of Energy (DOE) Office of Science User Facility operated for the DOE Office of Science by Argonne National Laboratory under Contract No. DE-AC02-06CH11357. C.F. acknowledges funding from the Danish Councils for Independent Research.

References

Allison et al., 1990

Allison J. D., Brown D. S. and Novo-Gradac K. J. (1990) MINTEQA2/PRODEFA2—A Geochemical Assessment Model for Environmental Systems: Version 3.0 User's Manual. U.S. Environmental Protection Agency, Athens, Georgia.

Aradóttir et al., 2012

E.S.P. Aradóttir, E.L. Sonnenthal, G. Björnsson, H. Jónsson**Multidimensional reactive transport modeling of CO_2 mineral sequestration in basalts at the Hellisheidi geothermal field, Iceland**

Int. J. Greenhouse Gas Control, 9 (2012), pp. 24-40

ArticleDownload PDFView Record in Scopus

Azoulay et al., 2012

I. Azoulay, C. Rémazeilles, P. Refait**Determination of standard Gibbs free energy of formation of chukanovite and Pourbaix diagrams of iron in carbonated media**

Corr. Sci., 58 (2012), pp. 229-236

ArticleDownload PDFView Record in Scopus

Berner and Kothavala, 2001

R.A. Berner, Z. Kothavala**GEOCARB III: a revised model of atmospheric CO_2 over phanerozoic time**

Am. J. Sci., 301 (2001), pp. 182-204

CrossRefView Record in Scopus

Berner et al., 1983

R.A. Berner, A.C. Lasaga, R.M. Garrels**The carbonate-silicate geochemical cycle and its effect on atmospheric carbon-dioxide over the past 100 million years**

Am. J. Sci., 283 (1983), pp. 641-683

CrossRefView Record in Scopus

Chupas et al., 2003

P.J. Chupas, X. Qiu, J.C. Hanson, P.L. Lee, C.P. Grey, S.J.L. Billinge**Rapid Acquisition Pair Distribution Function (RA-PDF) Analysis**

J. Appl. Crystallogr., 36 (2003), pp. 1342-1347

CrossRefView Record in Scopus
Clavaguera-Mora et al., 2002
M.T. Clavaguera-Mora, N. Clavaguera, D. Crespo, T. Pradell**Crystallisation kinetics and microstructure development in metallic systems**
Prog. Mater. Sci., 47 (2002), pp. 559-619
ArticleDownload PDFView Record in Scopus
Cornell and Schwertmann, 2003
R.M. Cornell, U. Schwertmann**The Iron Oxides: Structure, Properties, Reactions, Occurrences and Uses**
Wiley VCH, New York (2003)
Demichelis et al., 2011
R. Demichelis, P. Raiteri, J.D. Gale, D. Quigley, D. Gebauer**Stable prenucleation mineral clusters are liquid-like ionic polymers**
Nat. Commun., 2 (2011), p. 590, 10.1038/ncomms1604
Dong et al., 2000
H. Dong, J.K. Fredrickson, D.W. Kennedy, J.M. Zachara, R.K. Kukkadapu, T.C. Onstott**Mineral transformation associated with the microbial reduction of magnetite**
Chem. Geol., 169 (2000), pp. 299-318
ArticleDownload PDFView Record in Scopus
Duckworth and Martin, 2004
O.W. Duckworth, S.T. Martin**Role of molecular oxygen in the dissolution of siderite and rhodochrosite**
Geochim. Cosmochim. Acta, 68 (2004), pp. 607-621
ArticleDownload PDFView Record in Scopus
Ellwood et al., 1988
B.B. Ellwood, T.H. Chrzanowski, F. Hrouda, G.J. Long, M.L. Buhl**Siderite formation in anoxic deep-sea sediments – a synergetic bacterially controlled process with important implications in paleomagnetism**
Geology, 16 (1988), pp. 980-982
CrossRefView Record in Scopus
Farrow et al., 2007
C.L. Farrow, P. Juhas, J.W. Liu, D. Bryndin, E.S. Božin, J. Bloch, Th.Proffen, S.J.L. Billinge**PDFfit2 and PDFgui: computer programs for studying nanostructure in crystals**
J. Phys.: Condens. Matter, 19 (2007), p. 7, 10.1088/0953-8984/19/33/335219
View Record in Scopus
Forester and Koon, 1969
D.W. Forester, N.C. Koon**Mössbauer investigation of metamagnetic $FeCO_3$**
J. Appl. Phys., 40 (1969), pp. 1316-1317
CrossRefView Record in Scopus
Fredrickson et al., 1998
J.K. Fredrickson, J.M. Zachara, D.W. Kennedy, H.L. Dong, T.C.Onstott, N.W. Hinman, S.M. Li**Biogenic iron mineralization accompanying the dissimilatory reduction of hydrous ferric oxide by a groundwater bacterium**
Geochim. Cosmochim. Acta, 62 (1998), pp. 3239-3257
ArticleDownload PDFView Record in Scopus
Gebauer et al., 2008
D. Gebauer, A. Volkel, H. Colfen**Stable prenucleation calcium carbonate clusters**

Science, 322 (2008), pp. 1819-1822
CrossRefView Record in Scopus
Gilbert and Wilt, 2011
P.U.P.A. Gilbert, F.H. Wilt

W.E.G. Müller (Ed.), Molecular Biomineralization: Aquatic Organisms Forming Extraordinary Materials, Springer, New York (2011), pp. 199-223

CrossRefView Record in Scopus
Gislason and Oelkers, 2014
S.R. Gislason, E.H. Oelkers**Carbon storage in basalt**
Science, 344 (2014), pp. 373-374
CrossRefView Record in Scopus
Gislason et al., 2010
S.R. Gislason, D. Wolff-Boenisch, A. Stefansson, E.H. Oelkers, E.Gunnlaugsson, H. Sigurdardottir, B. Sigfusson, W.S. Broecker, J.M. Matter, M. Stute, G. Axelsson, T. Fridriksson**Mineral sequestration of carbon dioxide in basalt: a pre-injection overview of the CarbFix project**
Int. J. Greenh. Gas Con., 4 (2010) (2010), pp. 537-545
ArticleDownload PDFView Record in Scopus
Graf, 1961
D.L. Graf**Crystallographic tables for the rhombohedral carbonates**
Am. Min., 46 (1961), pp. 1283-1316
View Record in Scopus
Grosvenor et al., 2004
A.P. Grosvenor, B.A. Kobe, N.S. McIntyre**Studies of the oxidation of iron by water vapour using X-ray photoelectron spectroscopy and QUASE™**
Surf. Sci., 572 (2004), pp. 217-227
ArticleDownload PDFView Record in Scopus
Gu et al., 1999
B. Gu, T.J. Phelps, L. Liang, M.J. Dickey, Y. Roh, B.L. Kinsall, A.V. Palumbo, G.K. Jacobs**Biogeochemical dynamics in zero-valent iron columns: implications for permeable reactive barriers**
Environ. Sci. Technol., 33 (1999), pp. 2170-2177
CrossRefView Record in Scopus
Hammersley, 1997
Hammersley A. P. (1997) FIT2D: An Introduction and Overview. ESRF Internal Report, ESRF97HA02T. Available at http://www.esrf.eu/computing/scientific/FIT2D/FIT2D_INTRO/fit2d.html.
Hammersley et al., 1994
A.P. Hammersley, S.O. Svensson, A. Thompson**Calibration and correction of spatial distortions in 2D detector systems**
Nucl. Instr. Meth., A346 (1994), pp. 312-321
ArticleDownload PDFView Record in Scopus
Heuer and Stubbins, 1999
J.K. Heuer, J.F. Stubbins**An XPS characterization of $FeCO_3$ films from CO_2 corrosion**
Corr. Sci., 41 (1999), pp. 1231-1243

ArticleDownload PDFView Record in Scopus
Hulbert, 1969
S.F. Hulbert**Models for solid-state reactions in powdered compacts: a review**
J. Brit. Ceram. Soc., 6 (1969), pp. 11-20
View Record in Scopus
Ithurbide et al., 2009
A. Ithurbide, S. Peulon, F. Miserque, C. Beaucaire, A. Chausse, C.Poinssot**Electrophoretic deposition of siderite thin layers: influence of electrode potential and deposition time**
Thin Solid Films, 518 (2009), pp. 2644-2648
Johnson et al., 2005
C.M. Johnson, E.E. Roden, S.A. Welch, B.L. Beard**Experimental constraints on Fe isotope fractionation during magnetite and Fe carbonate formation coupled to dissimilatory hydrous ferric oxide reduction**
Geochim. Cosmochim. Acta, 69 (2005), pp. 963-993
ArticleDownload PDFView Record in Scopus
Kooi, 2006
B.J. Kooi**Extension of the Johnson-Mehl-Avrami-Kolmogorov theory incorporating anisotropic growth studied by Monte Carlo simulations**
Phys. Rev. B, 73 (2006), p. 054103
CrossRef
Konhauser et al., 2007
K.O. Konhauser, L. Amskold, S.V. Lalonde, N.R. Posth, A. Kappler, A.Anbar**Decoupling photochemical Fe(II) oxidation from shallow-water BIF deposition**
Earth Planet. Sci. Lett., 258 (2007), pp. 87-100
ArticleDownload PDFView Record in Scopus
Kukkadapu et al., 2005
R.K. Kukkadapu, J.M. Zachara, J.K. Fredrickson, D.W. Kennedy, A.C.Dohnalkova, D.E. McCready**Ferrous hydroxy carbonate is a stable transformation product of biogenic magnetite**
Am. Min., 90 (2005), pp. 510-515
CrossRefView Record in Scopus
Liu et al., 2001
C.X. Liu, S. Kota, J.M. Zachara, J.K. Fredrickson, C.K. Brinkman**Kinetic analysis of the bacterial reduction of goethite**
Environ. Sci. Technol., 35 (2001), pp. 2482-2490
CrossRefView Record in Scopus
Michel et al., 2007
F.M. Michel, L. Ehm, S.M. Antao, P.L. Lee, P.J. Chupas, G. Liu, D.R.Strongin, M.A.A. Schoonen, B.L. Phillips, J.B. Parise**The structure of ferrihydrite, a nanocrystalline material**
Science, 316 (2007), pp. 1726-1729
CrossRefView Record in Scopus
Michel et al., 2008
F.M. Michel, J. MacDonald, J. Feng, B.L. Phillips, L. Ehm, C. Tarabrella, J.B. Parise, R.J. Reeder**Structural characteristics of synthetic amorphous calcium carbonate**
Chem. Mater., 20 (2008), pp. 4720-4728
CrossRefView Record in Scopus

Michel et al., 2010
F.M. Michel, V. Barrón, J. Torrent, M.P. Morales, C.J. Serna, J-F. Boily, Q.Liu, A. Ambrosini, A.C. Cismasu, Jr.G.E. Brown**Ordered ferrimagnetic form of ferrihydrite reveals links among structure, composition, and magnetism**
PNAS, 107 (2010), pp. 2787-2792
CrossRefView Record in Scopus
Mozley, 1989
P.S. Mozley**Relation between depositional environment and the elemental composition of early diagenetic siderite**
Geology, 17 (1989), pp. 704-706
CrossRefView Record in Scopus
Mortimer et al., 1997
R.J.G. Mortimer, M.L. Coleman, J.E. Rae**Effect of bacteria on the elemental composition of early diagenetic siderite: implications for palaeoenvironmental interpretations**
Sedimentology, 44 (1997), pp. 759-765
View Record in Scopus
Neff et al., 2005
D. Neff, P. Dillmann, L. Bellot-Gurlet, G. Beranger**Corrosion of iron archaeological artefacts in soil: characterisation of the corrosion system**
Corr. Sci., 47 (2005), pp. 515-535
ArticleDownload PDFView Record in Scopus
Nielsen et al., 2014
M.H. Nielsen, S. Aloni, J.J. De Yoreo**In situ TEM imaging of $CaCO_3$ nucleation reveals coexistence of direct and indirect pathways**
Science, 345 (2014), pp. 1158-1162
CrossRefView Record in Scopus
Oelkers et al., 2008
E.H. Oelkers, S.R. Gislason, J. Matter**Mineral carbonation of CO_2**
Elements, 4 (2008), pp. 333-337
CrossRefView Record in Scopus
Ohmoto et al., 2004
H. Ohmoto, Y. Watanabe, K. Kumazawa**Evidence from massive siderite beds for a CO_2-rich atmosphere before, 1.8 billion years ago**
Nature, 429 (2004), pp. 395-399
CrossRefView Record in Scopus
Parkhurst and Appelo, 1999
Parkhurst D. L. and Appelo C. A. J. (1999) User's guide to PHREEQC (version 2) – a computer program for speciation, batch-reaction, one-dimensional transport, and inverse geochemical calculations. Water-Resources Investigations Report 99–4259. U.S. Geological Survey, Denver.
Pekov et al., 2007
I.V. Pekov, N. Perchiazzi, S. Merlino, N. Vyacheslav, M. Merlini, A.E. Zadov**Chukanovite, $Fe_2(CO_3)(OH)_2$, a new mineral from the weathered iron meteorite Dronino**
Eur. J. Mineral., 19 (2007), pp. 891-898
CrossRefView Record in Scopus
Pouget et al., 2009

E.M. Pouget, P.H.H. Bomans, J. Goos, P.M. Frederik, G. de With, N.Sommerdijk**The initial stages of template-controlled $CaCO_3$ formation revealed by Cryo-TEM**
Science, 323 (2009), pp. 1455-1458
CrossRefView Record in Scopus
Pye, 1984
K. Pye**SEM analysis of siderite cements in intertidal marsh sediments, Norfolk, England**
Mar. Geol., 56 (1984), pp. 1-12
ArticleDownload PDFView Record in Scopus
Qiu and Thompson, 2004
X. Qiu, J.W. Thompson**PDFgetX2: a GUI-driven program to obtain the pair distribution function from X-ray powder diffraction data**
J. Appl. Crystallogr., 37 (2004), pp. 110-116
CrossRefView Record in Scopus
Radha et al., 2012
A.V. Radha, A. Fernandez-Martinez, Y.D. Hu, Y.S. Jun, G.A. Waychunas, A. Navrotsky**Energetic and structural studies of amorphous $Ca_{1-x}Mg_xCO_3 \cdot nH_2O$ ($0 \leqslant x \leqslant 1$)**
Geochim. Cosmochim. Acta, 90 (2012), pp. 83-95
ArticleDownload PDFView Record in Scopus
Rakovan et al., 1999
J. Rakovan, U. Becker, M.F. Hochella**Aspects of goethite surface microtopography, structure, chemistry, and reactivity**
Am. Min., 84 (1999), pp. 884-894
CrossRefView Record in Scopus
Rodriguez-Blanco et al., 2008
J.D. Rodriguez-Blanco, S. Shaw, L.G. Benning**How to make 'stable' ACC: protocol and preliminary structural characterization**
Min. Mag., 72 (2008), pp. 283-286
CrossRefView Record in Scopus
Roh et al., 2003
Y. Roh, C.L. Zhang, H. Vali, R.J. Lauf, J. Zhou, T.J. Phelps**Biogeochemical and environmental factors in Fe biomineralization: magnetite and siderite formation**
Clays Clay Miner., 51 (2003), pp. 83-95
CrossRefView Record in Scopus
Sánchez-Román et al., 2014
M. Sánchez-Román, D. Fernández-Remolar, R. Amils, A.Sánchez-Navas, T. Schmid, P.S. Martin-Uriz, N. Rodríguez, J.A. McKenzie, C.Vasconcelos**Microbial mediated formation of Fe-carbonate minerals under extreme acidic conditions**
Sci. Rep., 4 (2014), 10.1038/srep04767
Sel et al., 2012
O. Sel, A.V. Radha, K. Dideriksen, A. Navrotsky**Amorphous iron (II) carbonate: crystallization energetics and comparison to other carbonate minerals related to CO_2 sequestration**
Geochim. Cosmochim. Acta, 87 (2012), pp. 61-68
ArticleDownload PDFView Record in Scopus
Shannon, 1976

R.D. Shannon**Revised effective ionic radii and systematic studies of interatomic distances in halides and chalcogenides**
Acta Cryst. A, 32 (1976), pp. 751-767
CrossRefView Record in Scopus
Sjöberg and Rickard, 1984
E.L. Sjöberg, D.T. Rickard**Temperature dependence of calcite dissolution kinetics between 1 and 62 °C at pH 2.7 to 8.4 in aqueous solutions**
Geochim. Cosmochim. Acta, 48 (1984), pp. 485-493
ArticleDownload PDFView Record in Scopus
Starink, 2001
M.J. Starink**On the meaning of the impingement parameter in kinetic equations for nucleation and growth reactions**
J. Mater. Sci., 36 (2001), pp. 4433-4441
CrossRefView Record in Scopus
Steefel and Van Cappellen, 1990
C.I. Steefel, P. Van Cappellen**A new kinetic approach to modeling water-rock interaction: the role of nucleation, precursors, and Ostwald ripening**
Geochim. Cosmochim. Acta, 54 (1990), pp. 2657-2677
ArticleDownload PDFView Record in Scopus
Stipp and Hochella, 1991
S.L. Stipp, M.F. Hochella**Structure and bonding environments at the calcite surface as observed with x-ray photoelectron-spectroscopy (xps) and low-energy electron-diffraction (leed)**
Geochim. Cosmochim. Acta, 55 (1991), pp. 1723-1736
ArticleDownload PDFView Record in Scopus
Wallace et al., 2013
A.F. Wallace, L.O. Hedges, A. Fernandez-Martinez, P. Raiteri, J.D. Gale, G.A. Waychunas, S. Whitelam, J.F. Banfield, J.J. De Yoreo**Microscopic Evidence for Liquid-Liquid Separation in Supersaturated $CaCO_3$ Solutions**
Science (2013), pp. 885-889
CrossRefView Record in Scopus
Wedepohl, 1995
K.H. Wedepohl**The composition of the continental-crust**
Geochim. Cosmochim. Acta, 59 (1995), pp. 1217-1232
View Record in Scopus
Wiesli et al., 2004
R.A. Wiesli, B.L. Beard, C.M. Johnson**Experimental determination of Fe isotope fractionation between aqueous Fe(II), siderite and “green rust” in abiotic systems**
Chem. Geol., 211 (2004), pp. 343-362
ArticleDownload PDFView Record in Scopus
Wyckoff, 1963
R.W.G. Wyckoff**Crystal Structures**
(Second edition), Interscience Publishers, New York, New York (1963), pp. 239-444
View Record in Scopus
Yee et al., 2006

N. Yee, S. Shaw, L.G. Benning, T.H. Nguyen**The rate of ferrihydrite transformation to goethite via the Fe(II) pathway**
Am. Min., 91 (2006), pp. 92-96
CrossRefView Record in Scopus